AGU ADVANCING EARTH AND SPACE SCIENCE

Geophysical Research Letters®

RESEARCH LETTER
10.1029/2021GL096699

A Broadband View of the Sea Surface Height Wavenumber Spectrum

Ana B. Villas Bôas[1,2,3], Luc Lenain[3], Bruce D. Cornuelle[3], Sarah T. Gille[3], and Matthew R. Mazloff[3]

[1]California Institute of Technology, La Jolla, CA, USA, [2]Colorado School of Mines, Golden, CO, USA, [3]Scripps Institution of Oceanography, University of California San Diego, La Jolla, CA, USA

Key Points:

- We present unique broadband airborne lidar observations of sea surface height spanning scales from hundreds of kilometers to a few meters
- The sea surface height variance due to surface waves can be over an order of magnitude larger than the variance at submesoscales
- The observed sea surface height is sensitive to the direction of waves which may impact the interpretation of remote sensing measurements

Supporting Information:

Supporting Information may be found in the online version of this article.

Correspondence to:

A. B. Villas Bôas,
villasboas@mines.edu

Citation:

Villas Bôas, A. B., Lenain, L., Cornuelle, B. D., Gille, S. T., & Mazloff, M. R. (2022). A broadband view of the sea surface height wavenumber spectrum. *Geophysical Research Letters*, *49*, e2021GL096699. https://doi.org/10.1029/2021GL096699

Received 22 OCT 2021
Accepted 31 JAN 2022

Author Contributions:

Conceptualization: Ana B. Villas Bôas, Luc Lenain
Formal analysis: Ana B. Villas Bôas
Funding acquisition: Luc Lenain, Bruce D. Cornuelle, Sarah T. Gille, Matthew R. Mazloff
Methodology: Ana B. Villas Bôas, Luc Lenain, Bruce D. Cornuelle, Sarah T. Gille, Matthew R. Mazloff
Software: Ana B. Villas Bôas
Supervision: Bruce D. Cornuelle, Sarah T. Gille, Matthew R. Mazloff
Visualization: Ana B. Villas Bôas

Abstract Airborne lidar altimetry can measure the sea surface height (SSH) over scales ranging from hundreds of kilometers to a few meters. Here, we analyze the spectrum of SSH observations collected during an airborne lidar campaign conducted off the California coast. We show that the variance in the surface wave band can be over 20 times larger than the variance at submesoscales and that the observed SSH variability is sensitive to the directionality of surface waves. Our results support the hypothesis that there is a spectral gap between meso-to-submesoscale motions and small-scale surface waves and also indicate that aliasing of surface waves into lower wavenumbers may complicate the interpretation of SSH spectra. These results highlight the importance of better understanding the contributions of different physics to the SSH variability and considering the SSH spectrum as a continuum in the context of future satellite altimetry missions.

Plain Language Summary Using unique measurements of the sea surface height (SSH) taken from an instrument onboard an airplane off the California coast, we examine how the variance of the SSH is distributed across different spatial scales, ranging from hundreds of kilometers to a few meters. We show that surface waves can be 20 times more energetic than motions with larger scales (known as submesocales) and that the direction of surface waves impacts the SSH variability depending on different sampling and averaging strategies. These results highlight the importance of better understanding the contributions of different types of motions and physics to the SSH variability. In particular, we advocate measuring scales from meters to hundreds of kilometers as a continuum to better inform future satellite altimetry missions.

1. Introduction

Since the launch of ERS-1 in 1991, a sequence of satellites equipped with altimeters have continuously observed sea surface height (SSH) at global scales. Although satellite altimetry has changed our understanding of many oceanographic phenomena at large and mesoscales (e.g., El Niño, Rossby waves, mesoscale eddies), the temporal and spatial resolution of the present constellation is insufficient to observe the two-dimensional structure of SSH variability at scales shorter than 150 km (Morrow et al., 2019). The upcoming Surface Water and Ocean Topography (SWOT) mission will change this paradigm by mapping the sea surface via two parallel 50-km-wide swaths, capable of resolving processes with wavelengths as small as ∼15 km.

Recent work motivated by SWOT has explored the different dynamical processes that contribute to the sea surface height variability at meso (100–300 km) and large submesoscales (15−100 km). Observational and numerical studies focusing both on regions of strong baroclinic jets (e.g., Callies et al., 2015; Qiu et al., 2018; Rocha, Chereskin, et al., 2016) and less energetic currents (e.g., Chereskin et al., 2019), have found SSH spectra consistent with quasi-geostrophic (QG) turbulence theory, which predicts a wavenumber (k) spectrum that decays with a spectral slope ranging from k^{-5} to $k^{-11/3}$ for wavenumbers in the mesoscale-to-submesoscale range. However, for spatial scales shorter than the so-called "transition scale" (Qiu et al., 2018), inertia-gravity waves (IGWs) play an important role in SSH variability, and the spectral slope of the SSH spectrum is typically shallower than the QG turbulence prediction of $k^{-11/3}$ (Rocha, Gille, et al., 2016; Qiu et al., 2017). Here, we refer to the low-wavenumber region of the SSH spectrum, that has a clear negative spectral slope, as the *red zone* (Figure 1, left).

Beyond this transition scale, at wavelengths ranging from tens of kilometers to a few kilometers, multiple dynamical processes such as internal waves, submesocale fronts, infra-gravity waves, and surface wave groups are expected to contribute to the SSH wavenumber spectrum; however, the lack of observations in this range of wavenumbers makes it difficult to understand the role of each process, and results from numerical ocean models

Writing – original draft: Ana B. Villas Bôas
Writing – review & editing: Luc Lenain, Bruce D. Cornuelle, Sarah T. Gille, Matthew R. Mazloff

at these scales are yet to be validated. In this paper, we refer to this range of wavenumbers as the *gray zone* (Figure 1, center).

At scales ranging from hundreds of meters to a few meters, the wavenumber spectrum of the sea surface elevation is dominated by surface gravity waves. Surface wave frequency spectra are routinely measured by wave buoys. Although these measured values can be converted to wavenumber spectra by applying the linear dispersion relationship of surface waves, the directional and wavenumber information from pitch-roll buoys is limited, especially at high-wavenumbers (Lenain & Melville, 2017). A typical surface wave spectrum displays a clear peak (or peaks) corresponding to the dominant surface gravity wavelength. For wavelengths longer than the peak, the spectrum is blue, that is, with variance increasing with higher wavenumbers. For wavelengths shorter than the peak, the spectrum is red, indicating that variance decreases as a function of wavenumber for these scales smaller than the gravity wave peak. The number of peaks depends on the local wind conditions and the exposure to remotely generated swell. Multiple peaks indicate the superposition of multiple wave systems. We will refer to the entire surface wave band as the *blue zone* (Figure 1, right).

Because there is a clear scale separation between QG turbulence and surface wave dynamics, these two spectral bands (red and blue) have been traditionally explored independently. SWOT will, for the first time, resolve the 2D variability on scales at which some of these processes overlap (the gray zone); thus, there is a need to better understand the contribution of different physics to the SSH variability and consider the SSH spectrum as a continuum.

Using laser-altimetry SSH measurements from the Ice, Cloud, and land Elevation Satellite 2 (ICESat-2), Yu et al. (2021) analyzed the spectrum of SSH in the Tropical Pacific at scales ranging from 500 km to 50 m, and also classified the spectrum into three distinct spectral bands. However, the one-dimensional nature of the ICESat-2 measurements, which has a typical footprint of 15 m, does not resolve the directional distribution of surface waves, limiting the interpretation of the SSH spectrum on that study. While Yu et al. (2021) relied on synthetic SSH to explore potential sampling issues that could lead to the SSH observed by ICESat-2, here we use a set of scanning airborne lidar swath measurements to show for the first time a broadband view of the SSH wavenumber spectrum spanning scales from hundreds of kilometers to a few meters, while simultaneously resolving the directional spectrum of surface waves during distinct wave and wind conditions.

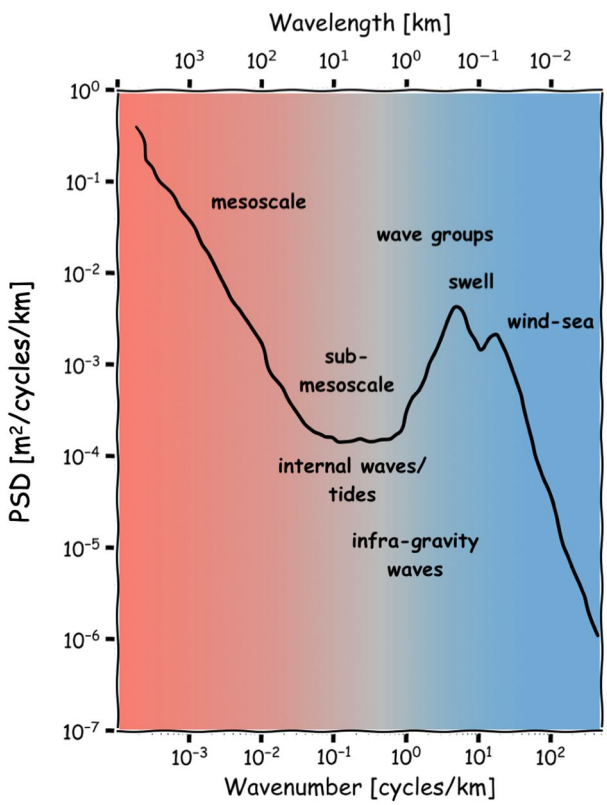

Figure 1. Schematic representation of a broadband spectrum of the sea surface height (SSH). The shading on the background indicates the three different spectral zones defined in this paper: red, gray, and blue zones. Words (in black) indicate the main physical processes that contribute to the SSH variance on each zone.

This paper is organized as follows. In Section 2, we describe the data set and environmental conditions during an airborne lidar campaign in the California Current region. In Section 3, we use the lidar measurements to analyze the variance spectrum of across-track averaged SSH. Then, in Section 4, we take advantage of the directional spectrum in the surface wave band to explore potential implications of different sampling and averaging strategies to the structure of the SSH spectrum. Section 5 discusses potential implications for satellite altimetry and presents some summary points.

2. SWOT Prelaunch Airborne Campaign

Data used in this study were collected during the SWOT pre-launch airborne campaign that took place in the California Current region between 28 March and 10 April 2019. The objective of the pre-launch airborne campaign was to validate the integration and performance of the Scripps Institution of Oceanography (SIO) Modular Aerial Sensing System (MASS) in the NASA Johnson Space Center (JSC) Gulfstream V (G-V) research aircraft. The campaign flew over oceanic and terrestrial targets to gather information needed to plan future SWOT calibration and validation (CalVal) activities. In this study, we will focus on the 28 March and 9 April flights, which were characterized by distinct surface wave conditions.

Our analyses are based on measurements from the Riegl Q680i waveform scanning lidar on the SIO MASS, which provides spatio-temporal measurements of the sea surface elevation. The lidar scans the sea surface with a swath width typically ranging from a few hundreds of meters to a kilometer, proportional to the altitude of the aircraft and also dependent on the sea state and wind speed. We refer the reader to Melville et al. (2016) for more details on the MASS instruments and processing.

For each pass, the surface elevation data from the MASS lidar were georeferenced from aircraft to an Earth coordinate 3D point cloud. All analyses presented here are based on point cloud measurements after rotating the measurements to along-track and cross-track coordinates, and bin-averaging. For the SSH spectral analysis, the data were averaged onto regular 1 × 1 m bins. For the directional wave spectrum, the data were averaged onto regular 0.5 × 0.5 m bins, and a Doppler shift correction was applied to the wave spectrum to account for the relative motion between the phase speed of the waves and the aircraft motion (see Lenain & Melville, 2017).

2.1. Environmental Conditions

Environmental conditions for the 9 April 2019 flights are shown in Figure 2. Winds were much stronger in comparison with the 29 March flights (see Figure S1 in Supporting Information S1), with an average speed of 15 m s^{-1} near the coast and 11–13 m s^{-1} in the offshore region (Figure 2c, color shading and vectors). These strong northwesterly winds are characteristic of expansion fan wind events (Colosi et al., 2021; Villas Bôas et al., 2017) and resulted in mixed seas, with the superposition of a remotely generated swell with peak period, wavelength, and direction of 11.3 s, 200 m, and 308°, respectively, and a local wind-sea with peak period, wavelength, and direction of 6.1 s, 59 m, and 321°, as shown in the MASS directional wave spectrum (Figure 2a). The overall significant wave height was 3.1 m. The omnidirectional spectrum (integral of the directional spectrum over all directions) computed from the MASS directional spectrum shows good agreement with the spectra from nearby CDIP buoys (Figure 2b), in particular in comparison to CDIP 094, which is exposed to wind conditions similar to the experiment site. MASS sampled the sea surface along two quasiorthogonal tracks shown in Figure 2c, here referred to as up/down-wind tracks (black) and cross-wind tracks (gray). For the 9 April flights, there were a total of eight passes in the up/down-wind direction and six passes in the cross-wind direction, with an average swath

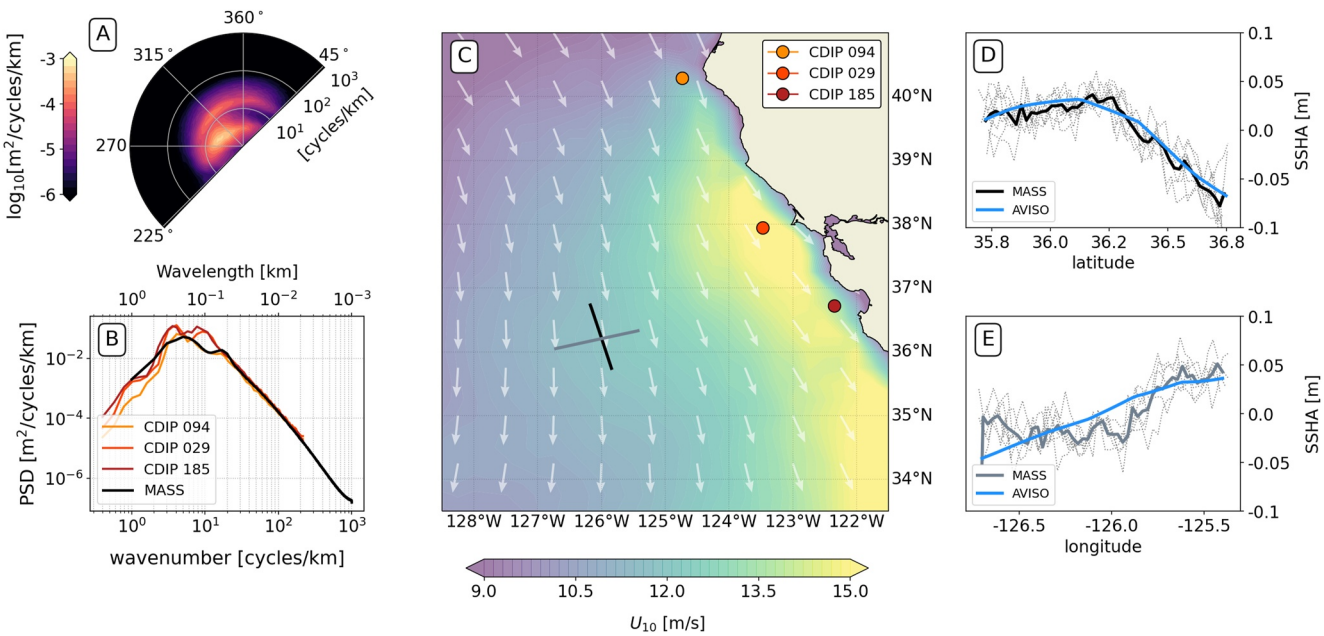

Figure 2. Environmental conditions during the 9 April 2019 flights. (a) Mean directional wave spectrum from Modular Aerial Sensing System (MASS). (b) Respective omnidirectional spectrum from MASS (black), CDIP buoys 094 (orange), 029 (red), and 185 (crimson). (c) Average Wind speed (colors) and direction (vectors) on 9 April 2019 from ERA5; MASS tracks for the up/down wind (Black) and cross wind (gray) are overlaid; The locations of CDIP wave buoys are shown as colored circles for 094 (orange), 029 (red), and 185 (crimson). (d) Across-track average sea surface height anomaly (SSHA) for each up/down-wind pass smoothed to 2.5 km (dotted); SSHA average across all passes (thick black); gridded SSHA from AVISO for 9 April 2019 interpolated to the MASS track coordinates (blue). (e) Same as (d) but for the cross-wind tracks.

width of 500 m. For each pass, the sea surface height anomaly (SSHA) was computed by applying tidal corrections and removing the mean sea surface (MSS) provided by the Collecte Localisation Satellites (CLS) group. The resulting cross-track averaged SSHA for each pass are shown as dotted lines in Figure 2d, (up/down-wind) and Figure 2e, (cross-wind), along with the average across all tracks (thick black and gray, respectively), and the corresponding gridded SSHA from AVISO interpolated to the up/down-wind and cross-wind tracks (light blue).

A similar figure for the 28 March 2019 flights is shown in the Supporting Information (Figure S1 in Supporting Information S1). Winds were relatively weak in the experiment region in comparison to the April flights, with average speed ranging from 6 m s^{-1} to 8 m s^{-1} and with predominantly westerly southwesterly directions (Figure S1c in Supporting Information S1, color shading and vectors). The sea state was dominated by one swell system with peak period of 9.6 s, peak direction of 285° (coming from the west/north-west), peak wavelength of 143 m, and significant wave height of 2.9 m. The omnidirectional spectrum from MASS also shows good agreement with the spectra measured by nearby CDIP wave buoys (Figure S1b in Supporting Information S1). For the 28 March flights, there were a total of nine passes in the up/down-wind direction and four passes in the cross-wind direction, with an average swath width of 200 m.

3. Spectral Analysis

In the following analysis, we investigate wavenumber spectra of across-track averaged SSHA for the 28 March and 9 April flights. For each flight day, the wavenumber spectrum was computed for each track separately after detrending and applying a Hanning window. To reduce the noise at high wavenumbers, all spectra were smoothed with a 20-point moving average at wavenumbers higher than 10^{-1} cycles/km. Finally, all spectra from up/down-wind tracks were averaged together to produce the mean up/down-wind spectrum. Similar processing was used for the cross-wind spectrum. Because our analysis of the SSH spectrum is based on a 1×1 m gridded point cloud, the Nyquist wavenumber is 5×10^2 cycles km^{-1}. Figure 3 shows the wavenumber spectra of across-track averaged SSHA from MASS for the 28 March flights for the up/down-wind tracks (black) and cross-wind tracks (gray). On the same plot, the spectrum computed from along-track AltiKa measurements that appears in Figure 14

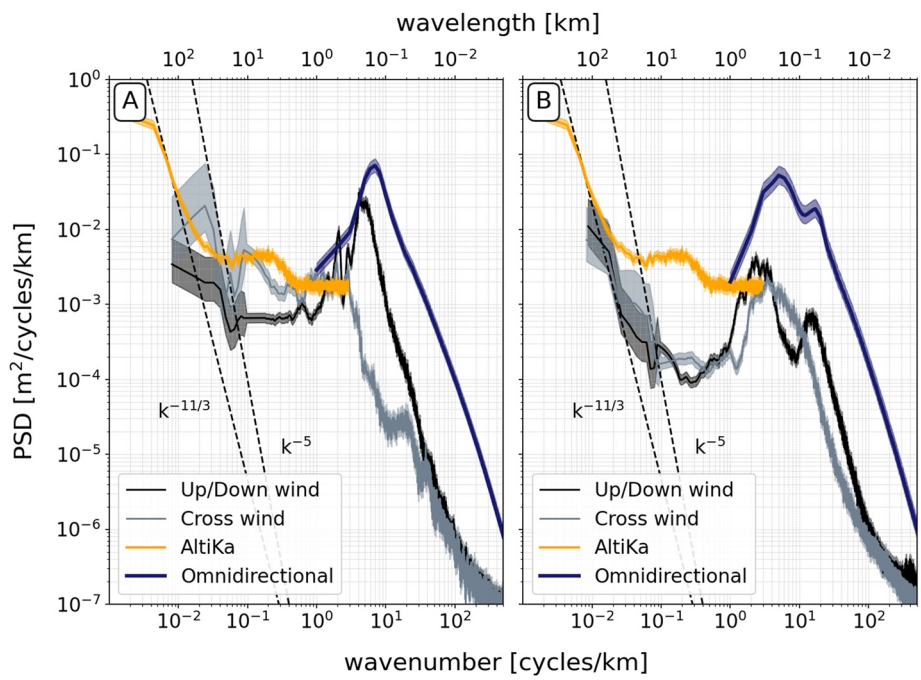

Figure 3. (a) Wavenumber spectrum of the cross-track averaged sea surface height anomaly (SSHA) from Modular Aerial Sensing System (MASS) for the 28 March 2019 flights. The spectrum averaged across all up/down-wind tracks is shown in black and the average cross-winds in gray. The same omnidirectional spectrum shown in Figure S1b in Supporting Information S1 is shown in dark purple. The mean wavenumber spectrum from Chereskin et al. (2019) computed using along-track AltiKa measurements off the California coast is shown in gold for reference. (b) Same as (a), but for the 10 April 2019 flights.

of Chereskin et al. (2019) is shown for reference (gold) as well as the omnidirectional wave spectrum from MASS (dark purple).

At low wavenumbers ($<10^{-1}$ cycles km^{-1}), the SSHA spectrum is red and has a spectral slope typical of mesoscale turbulence that falls between k^{-5} and $k^{-11/3}$, consistent with the AltiKa spectrum. In the gray zone the spectrum flattens out and becomes fairly white. At high wavenumbers (>1 cycle km^{-1}), the SSHA spectrum is blue, dominated by surface gravity waves, and at its peak is over 20 times more energetic than in the gray zone.

One important feature of Figure 3 is the remarkable difference between the omnidirectional spectrum, the across-track averaged spectrum in the up/down-wind direction, and across-track averaged spectrum in the cross-wind direction in the blue zone. Because of the highly anisotropic nature of the surface wavefield, averaging the 2D sea surface height in the across-track direction will result in significantly different spectra in the surface wave band. This distortion of the spectrum caused by the across-track averaging is dependent on the relative direction between the each wave component and the aircraft heading (or the azimuth direction) and can be illustrated using the following simple model.

Consider a monochromatic wave propagating in the (x, y) plane such that its surface elevation η is given by:

$$\eta(x, y) = A\sin\left(k_x x + k_y y\right), \tag{1}$$

where here x is the across-track (or range) direction, y is the along-track (or azimuth) direction, A is the wave amplitude and (k_x, k_y) are the across-track and along-track wavenumbers, respectively. The omnidirectional wavenumber is $K = \left(k_x^2 + k_y^2\right)^{1/2}$, and it will be kept fixed throughout this example.

If the monochromatic wave is propagating exactly in the along-track direction, then $k_x = 0$, $k_y = K$, and

$$\eta_\perp = A\sin\left(k_y y\right). \tag{2}$$

Averaging $\eta_\perp$ in the across-track direction over the swath width L leads to

$$\langle\eta_\perp\rangle = \frac{1}{L}\int_0^L A\sin\left(k_y y\right) dx = \eta_\perp, \tag{3}$$

which does not affect the sea surface elevation signal. If we now consider a "slanted" wave with the same omnidirectional wavenumber K, but propagating at an angle θ in respect to the along-track direction, the across-track averaging leads to

$$\begin{aligned}\langle\eta_\theta\rangle &= \frac{1}{L}\int_0^L A\sin\left(k_x x + k_y y\right) dx \\ &= -\frac{A}{k_x L}\left[\cos\left(k_x L + k_y y\right) - \cos\left(k_y y\right)\right] \\ &= \frac{2A}{k_x L}\sin\left(k_x L/2\right)\sin\left(k_x L/2 + k_y y\right).\end{aligned} \tag{4}$$

There are a few things to note from Equation 4. First, if the average is performed over a swath wide enough to span many wavelengths, then the amplitude of $\langle\eta_\theta\rangle$ is lower in comparison to $\langle\eta_\perp\rangle$. Second, the across-track averaged signal of the slanted wave $\langle\eta_\theta\rangle$ will appear as a longer wave, with wavenumber $k_y = \left(K^2 - k_x^2\right)^{1/2} = K\left(1 - k_x^2/K^2\right)^{1/2}$ which is lower in comparison to the wave propagating aligned with along-track direction. Third, for a fixed L, the attenuation of the wave amplitude by the averaging is non-linear in k_x. An illustration of the example discussed above is available as an interactive Jupyter Notebook in Villas Bôas (2022).

As shown in Figure S1a in Supporting Information S1, the wavefield during the 28 March flights was dominated by a single swell system coming from the west-northwest (285°), which is quasiparallel to the up/down-wind flight tracks (272°) and quasiorthogonal to the cross-wind tracks. As a result from the high relative angle between the cross-wind tracks and the dominant waves, the across-track averaged SSHA spectrum for the cross-wind tracks (Figure 3a, gray) has much lower variance in the surface wave band than the up/down-wind (black). The omnidirectional spectrum is shown in Figure 3a in dark purple. Note that, despite the relatively small angle between the aircraft heading and the peak swell direction for the up/down wind tracks ($\mathcal{O}10°$), the across-track

averaging results in a swell peak that is slightly shifted toward lower wavenumbers and has slightly lower variance in comparison to the omnidirectional spectrum.

The swath width for the April 9 flights was ~500 m, approximately twice the swath width of the March flights. The extra cross-track averaging on those tracks reduced the noise, leading to up/down-wind and cross-wind spectra that are indistinguishable from each other at low wavenumbers (Figure 3b) and that closely follow the AltiKa spectrum (gold line). Note that although SSHA variability in the blue zone is highly directional because of surface waves, we expect the spatial variability in the red zone to be somewhat isotropic (Chereskin et al., 2019).

The overall shape of the SSHA spectra in Figure 3b is similar to Figure 3a: a red spectrum with a spectral slope characteristic of QG turbulence at low wavenumbers flattens out in the gray zone (0.1–1 cycle km^{-1}) and becomes blue at wavenumbers higher than 1 cycle km^{-1}. Although it is challenging to identify precisely the processes contributing to the variance in the gray zone, we find that the variance in that band is consistent with what would be expected from internal waves and tides (Callies & Wu, 2019; Savage et al., 2017) and from infra-gravity waves (Ardhuin et al., 2014). In particular, free open ocean infragravity waves with horizontal wavelengths ranging from a few kilometers to tens of kilometers are expected to have spectral densities on the order of 10^{-4} m^2/cycle/km (Aucan & Ardhuin, 2013), which is in agreement with the results presented in Figure 3. The extent to which infragravity waves contribute to the observed SSH spectrum deserves further investigation and is beyond the scope of this manuscript.

The up/down-wind tracks (Figure 3b, black) were capable of capturing both the wind-sea and the swell peak in the surface wave band; however, since neither wave system (308° and 321°) is exactly aligned with the up/down-wind direction (342°), the peaks in the across-track averaged spectrum (black) are shifted toward lower wavenumbers and have lower variance in comparison to the omnidirectional spectrum (dark purple), especially the swell peak, which has higher angle relative to the along-track direction. For the tracks in the cross-wind direction, the across-track averaging spreads the variance from the wind-sea out to lower wavenumbers resulting in a spectrum that has a single, broader peak (Figure 3b, gray).

4. Filtering Surface Wave Signals

We have shown that the directionality of the surface wavefield may pose challenges for interpretating the SSH spectrum in the gray zone, since surface wave energy has the potential to be aliased into lower wavenumbers depending on sampling and averaging strategies. Radar altimeters effectively act as a filter, due to their relatively large footprint, while laser and SAR altimeters, might require further filtering to minimize wave effects. Thus, a natural question that arises is how the SSH would respond to different filtering scales and how much filtering would be necessary to effectively suppress the surface wave contribution to the SSH variability.

Figure 4 illustrates the transfer function of a Blackman–Harris window with three different feature resolutions, where the feature resolution L_r is defined as twice the distance at which the autocorrelation of the window drops to 0.5. For this example, the variance at the swell peak in the blue zone is about 15 dB higher than the variance in the gray zone. A filter with feature resolution of 250 m (Figure 4, light blue) would only attenuate that variance by 5 dB and would not be effective at removing the surface wave signal.

A consequence of this leftover high-wavenumber energy is that if the data were subsampled, for example, at 250 m posting, the energy that was not suppressed through filtering at wavenumbers higher than the Nyquist wavenumber (500 m) would be aliased to lower wavenumbers. Figure 4b illustrates this example using the SSHA from the April 9 flights for the up/down-wind tracks (left) and cross-wind tracks (right). The SSHA measurements were filtered with the same Blackman-Harris windows shown in Figure 4a, with feature resolution (L_r) of 250 m (light blue), 500 m (sky blue), and 1 km (dark blue), and then subsampled at 250 m. A filter with feature resolution of 500 m or longer (sky and dark blue) effectively attenuates the surface waves to prevent aliasing, while for L_r = 250 m more energy in the surface wave band remains to be folded into the high-wavenumber end of the red zone and the entire gray zone, resulting in a spectrum that is up to twice as energetic in that range (light blue). A similar discussion applies to spectra from the 28 March flights, shown in Figure S2 in Supporting Information S1.

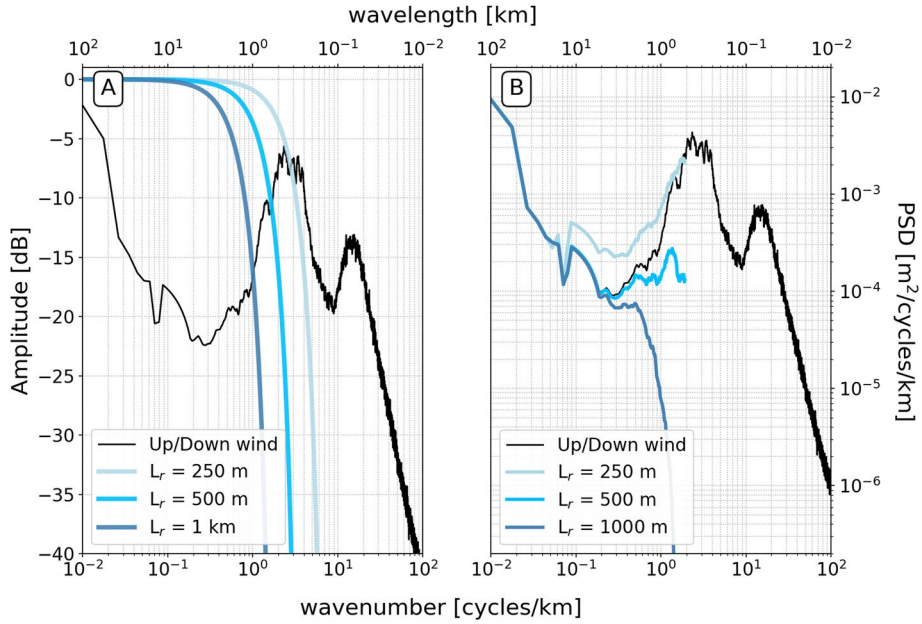

Figure 4. (a) Wavenumber spectrum of the cross-track averaged sea surface height anomaly (SSHA) from Modular Aerial Sensing System (MASS) for the 9 April 2019 flights (same as Figure 3b). The mean spectrum of the up/down-wind tracks is shown in black and the cross-wind tracks in gray. The colored lines are the transfer function of a Blackman-Harris window with feature resolution (see main text) of 250 m (light blue), 500 m (sky blue), and 1 km (dark blue). (b) Wavenumber spectrum of the cross-track averaged SSHA from MASS for the 9 April 2019 flights (same as Figure 3b). The mean spectrum of the up/down wind tracks is shown in black. The colored lines are the spectrum after filtering the signal with a Blackman-Harris window with feature resolution (L_r) of 250 m (light blue), 500 m (sky blue), and 1 km (dark blue), and subsampling at 250 m postings.

5. Discussion and Conclusions

In the context of present radar satellite altimetry, we are familiar with variability of sea surface height only down to wavelengths on the order of 100 km. At these scales, the idea of a red sea surface height spectrum, as shown in Figure 1, with a quasilinear spectral slope consistent with either surface or interior QG is widely accepted and has been observed in several regions of the ocean. The upcoming SWOT mission will provide for the first time an opportunity to observe processes at the high-wavenumber end of the red zone, down to wavelengths of a few 10s of kilometers. At these scales, ageostrophic motions such as inertia-gravity waves and infragravity waves are known to significantly contribute to the SSH variability and will present a challenge to interpreting high-resolution SSH (Aucan & Ardhuin, 2013; Rocha, Chereskin, et al., 2016; Savage et al., 2017).

SWOT will achieve much higher resolution than traditional altimetry by using synthetic aperture radar (SAR) interferometry to map the sea surface topography. At its most raw form, the SWOT SAR-KaRIn instrument will measure the sea surface with resolution of 2.5 m in the azimuth direction, and between 10 and 70 m in the range direction (Morrow et al., 2019). SWOT's unprecedented large volume of data will be unfeasible to downlink. Thus an onboard processor will preprocess the data by filtering each interferogram to achieve a feature resolution of 500 m both in the range and azimuth direction. For technical reasons, SWOT's onboard processor will apply a Blackman-Harris window in the azimuth direction, and Parzen window in the range direction. After filtering, blocks of nine interferograms will be downlinked at 250 m postings. On the ground, the interferometric data will be geolocated and combined to produce an "expert" product on a 250 × 250 m swath grid. In addition to the expert product, a 2 × 2 km product will also be available on a global grid.

The results discussed in the present manuscript highlight the often overlooked fact that the SSH spectrum becomes blue in the surface wave band. Our observations support the hypothesis that there is a spectral gap between meso-to-submesoscale motions (red zone) and small-scale surface waves, but also indicate that aliasing of surface waves into the less known gray zone can complicate interpretation of SSH spectra. In Southern California, where the wavefield is relatively weak in comparison to, for example, the North Atlantic or the Southern Ocean

(Stopa, 2021), we found that that the variance in the surface wave band can be over 20 times larger than the variance at the high-wavenumber end of the red zone (10–40 km). We showed that the directionality of the surface wavefield plays an important role in the measured SSH variability and that different sampling and processing strategies (e.g., across-track averaging) can lead to a shift of surface wave energy to lower wavenumbers. A similar discussion in the context of internal tides was carried out by Ray and Zaron (2016).

Based on the data that we analyzed here, the 500 m Blackman-Harris filtering planned for SWOT's onboard processor should be sufficient to suppress most surface wave energy and minimize aliasing effects. However, one has to be mindful that larger relative angles between the along-track direction and the dominant waves would shift the energy of the surface wave band to even lower wavenumbers, and in some cases significant surface wave energy might still remain after applying a 500 m filter. The potential for this effect to happen would vary seasonally and geographically with wave direction and amplitude. For example, in the target region for calibration and validation of SWOT, which overlaps with the MASS flights analyzed here, Villas Bôas et al. (2017) have shown that the significant wave height is above 3 m about 50% of time in the winter and it could reach over 5 m up to 10% of the time. The authors also show the during late spring and summer the distribution of the direction of the dominant waves is bimodal, with waves coming both from the south-southwest and north-northwest, which would translate into a broad range of relative angles between surface waves and SWOT's swath. It is important to note that other errors related to surface waves that are not discussed here, such as the so-called surfboard effect (Peral et al., 2015), are also expected to greatly impact the interpretation of SSH measurements from SWOT.

Finally, the type of analysis described in this paper has only been possible with detailed knowledge of the broadband two-dimensional SSH field measured by MASS. Although a need for high-resolution directional wave spectrum has been recognized by the oceanographic community (Ardhuin et al., 2019), there is currently no means of measuring high-resolution directional wave spectra globally. Surface waves play a major role in setting the sea surface geometry and variability (Villas Bôas & Pizzo, 2021). As spaceborne radar evolves toward resolving higher wavenumbers, surface wave measurements will become increasingly more important.

Data Availability Statement

The data used for this study are available through the UC San Diego Library Digital Collections at https://doi.org/10.6075/J0W0963R and it has been published as Villas Bôas et al. (2022). The source code used to produce the results from this paper is published as Villas Bôas (2022) and can be accessed in the following GitHub repository https://github.com/biavillasboas/BroadbandSpectrum as well as at https://www.doi.org/10.5281/zenodo.5866771.

Acknowledgments
A. B. Villas Bôas, S. T. Gille, B. D. Cornuelle, and M. R. Mazloff were funded by NASA award 80NSSC20K1136 through the SWOT program. A. B. Villas Bôas had additional funding from NASA award 80NSSC19K1004 through the S-MODE program. L. Lenain was funded through NASA JPL contract 1618801. The authors thank Nick Statom for collecting and preprocessing the data.

References

Ardhuin, F., Rawat, A., & Aucan, J. (2014). A numerical model for free infragravity waves: Definition and validation at regional and global scales. *Ocean Modelling*, *77*, 20–32. https://doi.org/10.1016/j.ocemod.2014.02.006

Ardhuin, F., Stopa, J. E., Chapron, B., Collard, F., Husson, R., Jensen, R. E., et al. (2019). Observing sea states. *Frontiers in Marine Science*, *6*, 124. https://doi.org/10.3389/fmars.2019.00124

Aucan, J., & Ardhuin, F. (2013). Infragravity waves in the deep ocean: An upward revision. *Geophysical Research Letters*, *40*(13), 3435–3439. https://doi.org/10.1002/grl.50321

Callies, J., Ferrari, R., Klymak, J. M., & Gula, J. (2015). Seasonality in submesoscale turbulence. *Nature Communications*, *6*(1), 1–8. https://doi.org/10.1038/ncomms7862

Callies, J., & Wu, W. (2019). Some expectations for submesoscale sea surface height variance spectra. *Journal of Physical Oceanography*, *49*(9), 2271–2289. https://doi.org/10.1175/jpo-d-18-0272.1

Chereskin, T. K., Rocha, C. B., Gille, S. T., Menemenlis, D., & Passaro, M. (2019). Characterizing the transition from balanced to unbalanced motions in the southern California Current. *Journal of Geophysical Research: Oceans*, *124*(3), 2088–2109. https://doi.org/10.1029/2018jc014583

Colosi, L. V., Villas Bôas, A. B., & Gille, S. T. (2021). The seasonal cycle of significant wave height in the ocean: Local versus remote forcing. *Journal of Geophysical Research: Oceans*, *126*(8), e2021JC017198. https://doi.org/10.1029/2021jc017198

Lenain, L., & Melville, W. K. (2017). Measurements of the directional spectrum across the equilibrium saturation ranges of wind-generated surface waves. *Journal of Physical Oceanography*, *47*(8), 2123–2138. https://doi.org/10.1175/jpo-d-17-0017.1

Melville, W. K., Lenain, L., Cayan, D. R., Kahru, M., Kleissl, J. P., Linden, P., & Statom, N. M. (2016). The modular aerial sensing system. *Journal of Atmospheric and Oceanic Technology*, *33*(6), 1169–1184. https://doi.org/10.1175/jtech-d-15-0067.1

Morrow, R., Fu, L.-L., Ardhuin, F., Benkiran, M., Chapron, B., Cosme, E., et al. (2019). Global observations of fine-scale ocean surface topography with the Surface Water and Ocean Topography (SWOT) mission. *Frontiers in Marine Science*, *6*. https://doi.org/10.3389/fmars.2019.00232

Peral, E., Rodríguez, E., & Esteban-Fernández, D. (2015). Impact of surface waves on SWOT's projected ocean accuracy. *Remote Sensing*, *7*(11), 14509–14529. https://doi.org/10.3390/rs71114509

Qiu, B., Chen, S., Klein, P., Wang, J., Torres, H., Fu, L.-L., & Menemenlis, D. (2018). Seasonality in transition scale from balanced to unbalanced motions in the world ocean. *Journal of Physical Oceanography*, *48*(3), 591–605. https://doi.org/10.1175/jpo-d-17-0169.1

Qiu, B., Nakano, T., Chen, S., & Klein, P. (2017). Submesoscale transition from geostrophic flows to internal waves in the northwestern Pacific upper ocean. *Nature Communications*, *8*(1), 1–10. https://doi.org/10.1038/ncomms14055

Ray, R. D., & Zaron, E. D. (2016). M2 internal tides and their observed wavenumber spectra from satellite altimetry. *Journal of Physical Oceanography*, *46*(1), 3–22. https://doi.org/10.1175/jpo-d-15-0065.1

Rocha, C. B., Chereskin, T. K., Gille, S. T., & Menemenlis, D. (2016). Mesoscale to submesoscale wavenumber spectra in Drake Passage. *Journal of Physical Oceanography*, *46*(2), 601–620. https://doi.org/10.1175/jpo-d-15-0087.1

Rocha, C. B., Gille, S. T., Chereskin, T. K., & Menemenlis, D. (2016). Seasonality of submesoscale dynamics in the Kuroshio extension. *Geophysical Research Letters*, *43*(21), 11–304. https://doi.org/10.1002/2016gl071349

Savage, A. C., Arbic, B. K., Alford, M. H., Ansong, J. K., Farrar, J. T., Menemenlis, D., et al. (2017). Spectral decomposition of internal gravity wave sea surface height in global models. *Journal of Geophysical Research: Oceans*, *122*(10), 7803–7821. https://doi.org/10.1002/2017jc013009

Stopa, J. E. (2021). Seasonality of wind speeds and wave heights from 30 years of satellite altimetry. *Advances in Space Research*, *68*(2), 787–801. https://doi.org/10.1016/j.asr.2019.09.057

Villas Bôas, A. B. (2022). *Source code for: A broadband view of the sea surface height wavenumber spectrum*. https://doi.org/10.5281/zenodo.5866771

Villas Bôas, A. B., Gille, S. T., Mazloff, M. R., & Cornuelle, B. D. (2017). Characterization of the deep water surface wave variability in the California Current region. *Journal of Geophysical Research: Oceans*, *122*(11), 8753–8769. https://doi.org/10.1002/2017jc013280

Villas Bôas, A. B., Lenain, L., & Statom, N. (2022). *Data for: A broadband view of the sea surface height wavenumber spectrum*. https://doi.org/10.6075/J0W0963R

Villas Bôas, A. B., & Pizzo, N. (2021). In K. Drushka, & M. Bourassa (Eds.), *The geometry, kinematics, and dynamics of the two-way coupling between wind, waves, and currents* (pp. 18–26). US CLIVAR. https://doi.org/10.5065/ybca-0s03

Yu, Y., Sandwell, D. T., Gille, S. T., & Villas Bôas, A. B. (2021). Assessment of ICESat-2 for the recovery of ocean topography. *Geophysical Journal International*, *226*(1), 456–467. https://doi.org/10.1093/gji/ggab084